Design of an ultra-broadband and fabrication-tolerant silicon polarization rotator splitter with SiO_2 top cladding

Xin Chen (陈 鑫)[1,3], Chao Qiu (仇 超)[2], Zhen Sheng (盛 振)[1,2], Aimin Wu (武爱民)[1,2,], Haiyang Huang (黄海阳)[1,3], Yingxuan Zhao (赵瑛璇)[1], Wei Li (李 伟)[1], Xi Wang (王 曦)[1], Shichang Zou (邹世昌)[1], and Fuwan Gan (甘甫烷)[1,2,*]**

[1]*State Key Laboratory of Functional Materials for Informatics, Shanghai Institute of Microsystem and Information Technology, Shanghai 200050, China*

[2]*Nantong Opto-Electronics Engineering Center Chinese Academy of Science, Nantong 226000, China*

[3]*University of Chinese Academy of Science, Beijing 100049, China*

**Corresponding author: fuwan@mail.sim.ac.cn; **corresponding author: wuaimin@mail.sim.ac.cn*

Received February 21, 2016; accepted June 14, 2016; posted online July 14, 2016

An ultra-broadband and fabrication-tolerant silicon polarization rotator splitter is proposed in this Letter. Benefitting from the broadband and low-loss characteristics of the bi-level taper and counter-tapered coupler, the designed device has a simulated insertion loss and crosstalk of less than 0.2 and −15 dB in the waveband from 1290 to 1610 nm. These characteristics make it valuable in applications with large bandwidth requirements, such as full-grid Coarse wavelength division multiplexer (CWDM) and diplexer/triplexer fiber-to-the-home systems. The fabrication tolerance of the design is also analyzed, showing that the device performance is quite stable with normal manufacturing errors in silicon photonics foundries.

OCIS codes: 130.3120, 130.5440.
doi: 10.3788/COL201614.081301.

On-chip optical interconnects based on silicon photonics technology have attracted significant attention in the past decade due to their compatibility with the mature complementary metal oxide semiconductor (CMOS) process, strong optical confinement, and the potential to realize the monolithic integration of optical and electronic components[1], which provide both cost and performance advantages. Several silicon photonic platforms have been demonstrated, and various optical interconnect devices have been developed[2–4]. The high level of integration also helps bring the design and production of systems into reality that otherwise would be too costly or complex to be developed in other material systems, such as wavelength division multiplexed passive optical network (WDM PON) solutions for fiber-to-the-home (FTTH)[5].

Coupling light from single-mode fibers to on-chip waveguides in silicon WDM PON systems requires large bandwidths and polarization insensitivity. Edge coupling of light from single-mode fibers to on-chip waveguides is typically utilized due to the narrow bandwidth drawback of grating couplers[6,7]. To further enable a polarization diversity operation, a broadband polarization splitter and rotator that cover the entire waveband from 1310 to 1550 nm are required[8]. An ultra-broadband polarization rotator splitter (PRS) operating from 1350 to 1750 nm was proposed in Ref. [9], in which they utilized a mode-sorting asymmetric Y-junction that requires high-resolution lithography and is difficult to precisely fabricate. Recently, a bi-wavelength PRS comprising an adiabatic TM_0-to-TE_1 conversion section and asymmetric directional coupler was proposed[8]; however, it is only suitable for FTTH applications at 1310 and 1550 nm wavebands and cannot satisfy the needs of triple wavebands in FTTH systems. A PRS with a bandwidth as large as 300 nm was proposed[10]. A layer of silicon nitride (Si_3N_4) was utilized as the top cladding material to break the vertical symmetry of the waveguides, which added complexity to the fabrication process.

In this Letter, we propose an ultra-broadband PRS based on a cascaded adiabatic bi-level taper and mode-evolution counter-tapered coupler. Benefitting from the broadband and low-loss characteristics of the adiabatic taper and counter-tapered coupler, the simulated insertion loss (IL) and crosstalk (CT) of the proposed PRS are less than 0.2 and −15 dB with a bandwidth as large as 320 nm, covering all 1310, 1490, and 1550 nm wavebands. A standard silicon dioxide (SiO_2) cladding is used without the introduction of silicon nitride or air cladding due to the asymmetric cross section of the rib waveguide. The fabrication process sensitivity of the device is also analyzed, showing a large fabrication tolerance with a waveguide width variation of ±40 nm and top silicon thickness or slab height variation of ±10 nm for the entire operation waveband. Considering the manufacturing deviations in industrial silicon photonic foundries that have a top silicon thickness variation of ±5 nm and linewidth variations <1%[11,12], this proposed device is quite fabrication tolerant. With such a broad operating bandwidth and a robust performance, this device offers great potential in silicon photonic systems, especially in applications requiring large bandwidths, such as WDM PONs for FTTH.

Figure 1 shows the schematic of the proposed device, where the dark blue regions represent the Si waveguides and light blue regions represent the partially etched slab

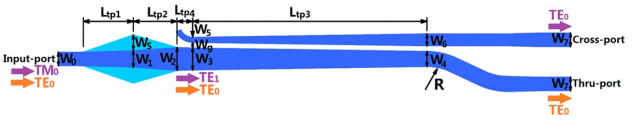

Fig. 1. Schematic of the proposed device based on a cascaded adiabatic bi-level taper and mode-evolution counter-tapered coupler.

waveguide. Table 1 lists the parameters and corresponding values of the proposed device. Silicon-on-insulator (SOI) wafers with a top silicon thickness H of 220 nm are used, and a slab height H_{slab} of 90 nm is selected to be compatible with the standard fabrication process in a silicon photonic foundry[13]. The device is composed of an adiabatic bi-level taper and a mode-evolution counter-tapered coupler. A standard SiO_2 top cladding is used due to the asymmetric cross section of the rib waveguide. Both the TE_0 and TM_0 modes are launched into the left port of the bus waveguide, as shown in Fig. 1. The TE_0 mode directly passes through the device and outputs from the through port. The TM_0 mode will be converted to the TE_1 mode first by the bi-level taper and then coupled to the TE_0 mode in the cross port after passing through the counter-tapered coupler. In this way, the TE_0 and TM_0 polarizations are separated and output as TE_0 modes at two ports. To obtain a broad operation bandwidth, both the bi-level taper and mode-evolution counter-tapered coupler are carefully optimized.

A bi-level taper with an asymmetrical waveguide cross section is utilized to realize a highly efficient TM_0-to-TE_1 mode conversion. Due to the mode hybridization in the asymmetric waveguide cross section, mode conversion between the TM fundamental mode and higher-order TE modes is observed[14]. To obtain a broad bandwidth covering the entire waveband from 1310 to 1550 nm, the device is optimized at two wavelengths of 1310 and 1550 nm. Effective indices of the first three modes (TE_0, TM_0, and TE_1) in the cross section along the proposed bi-level taper are calculated with a commercial simulation software package (FIMMWAVE) and shown in

Table 1. Parameters and Corresponding Values of the Proposed Device

Parameters	Values (μm)	Parameters	Values (μm)
W_0	0.45	W_s	0.5
W_1	0.55	W_g	0.16
W_2	0.75	L_{tp1}	28.5
W_3	0.72	L_{tp2}	25
W_4	0.5	L_{tp3}	200
W_5	0.18	L_{tp4}	10
W_6	0.4	R	20
W_7	0.45		

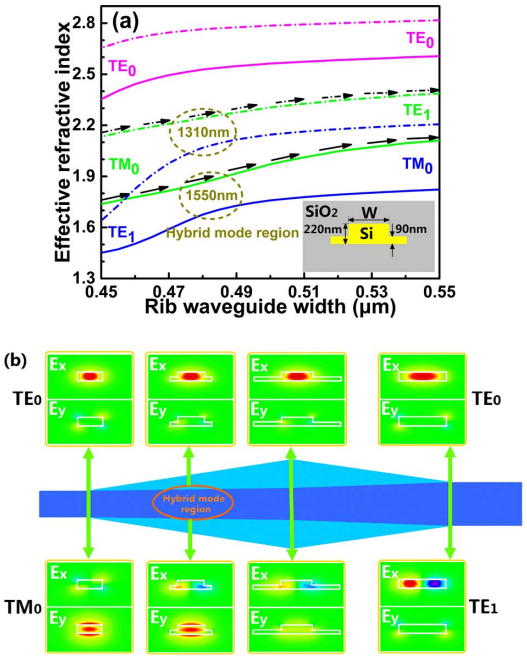

Fig. 2. (a) The calculated effective refractive indices of the first three modes in the waveguide cross section along the bi-level taper at wavelengths of 1310 nm (dashed) and 1550 nm (straight). (b) The electric field profiles of the first two modes in the cross section along this taper at the wavelength of 1310 nm.

Fig. 2(a). The brown dashed circles in Fig. 2(a) show the mode hybridizations between the TM_0 and TE_1 modes at the rib/slab waveguide widths around $W(0.48\ \mu\text{m})/W_s(0.15\ \mu\text{m})$ at the two wavelengths. A bi-level taper with rib widths/slab widths increased from $W_0(0.45\ \mu\text{m})/W_s(0\ \mu\text{m})$ to $W_1(0.55\ \mu\text{m})/W_s(0.5\ \mu\text{m})$ is designed. $W_1(0.55\ \mu\text{m})/W_s(0.5\ \mu\text{m})$ are selected to avoid the back conversion from the TE_1 mode to the TM_0 mode. The taper length L_{tp1} is also a factor determining W_1 and W_s. Figure 2(b) shows the electric field profiles of the first two modes in the cross section along this taper at the wavelength of 1310 nm. The first mode, which is identified as a TE_0 mode, directly passes the bi-level taper. The second mode is a TM_0 mode at the beginning of the taper and converted into a TE_1 mode after passing through the taper, which is also shown by straight and dashed arrows in Fig. 2(a). In the mode hybridization region, the minor component (E_x or E_y) is comparable to the corresponding major component (E_y or E_x), which leads to the mode conversion between the TM_0 and TE_1 modes[14], as shown in Fig. 2(b).

To obtain an efficient mode conversion, the taper lengths L_{tp1} and L_{tp2} need careful optimizations. The second taper with a length of L_{tp2} is designed after the conversion section to transform the rib waveguide to a channel one; this is shown in Fig. 1. The W_2 of 0.75 μm is selected such that the effective mode indices of the TE_1 and TM_0 modes are separated wide enough so that the TE_1 mode will not convert back to the TM_0 mode.

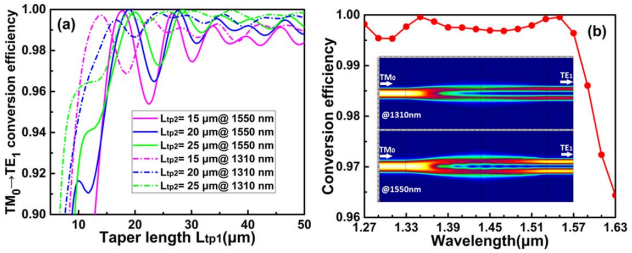

Fig. 3. (a) The mode conversion efficiency from the TM_0 mode to TE_1 mode in the bi-level taper as the L_{tp1} varies with the second taper length $L_{tp2} = 15$, 20, and 25 μm at the wavelength of 1310 nm (dashed) and 1550 nm (straight). (b) Wavelength dependence of the mode conversion efficiency when $L_{tp1} = 28.5$ μm and $L_{tp2} = 25$ μm. Inset: simulated electric field intensity distributions in the bi-level taper as the TM_0 mode launched at 1310 and 1550 nm wavelengths.

Meanwhile, a larger W_2 requires a longer taper to reduce the transition loss. The three-dimensional simulation software FIMMPROP based on the eigen-mode expansion (EME) method is used to find L_{tp1} and L_{tp2}. Figure 3(a) shows the simulated conversion efficiencies as a function of L_{tp1} with L_{tp2} of 15, 20, and 25 μm at both 1310 and 1550 nm wavelengths. The conversion efficiencies increase with increasing L_{tp1} for all three L_{tp2} and reach nearly 100% when L_{tp1} is large enough. One can also note that there are some notable ripples with a shorter L_{tp1} (<25 μm), which are likely caused by undesired modes interferences or reflections in the taper and could be eliminated with the increase of L_{tp1} and L_{tp2}. An L_{tp1} of 28.5 μm and an L_{tp2} of 25 μm are selected to achieve high efficiency mode conversions for the two wavelengths of 1310 and 1550 nm. The relation between conversion efficiency and wavelength is finally simulated with FIMMPROP and shown in Fig. 3(b). A conversion efficiency larger than 99% is obtained from the wavelength of 1.27 to 1.59 μm, which verified our design method using two wavelengths of 1310 and 1550 nm. The inset of Fig. 3(b) clearly shows the simulated electric field intensity distributions in this bi-level taper with the TM_0 mode launched at 1310 and 1550 nm wavelengths.

A counter-tapered coupler that has two waveguides with the cores counter tapered is designed after the bi-level taper to couple the obtained TE_1 mode in the bus waveguide to the TE_0 mode in the cross port. An adiabatic taper with a length of L_{tp4} is designed to connect the bi-level taper and counter-tapered coupler. The operation principle is based on mode evolution. Unlike the directional coupler based on interference theory, the counter-tapered couplers are approximate adiabatic devices and do not rely on precise phase conditions to be satisfied over an extended length, which permits ultra-wideband mode division operations. A more detailed discussion of the counter-tapered coupler can be found in Refs. [15,16]. An S-type bend with a radius of R is utilized to alleviate the coupling between the through and cross waveguides.

FIMMWAVE is used to calculate the effective indices of the TE_0 mode and TE_1 mode in the through waveguide and

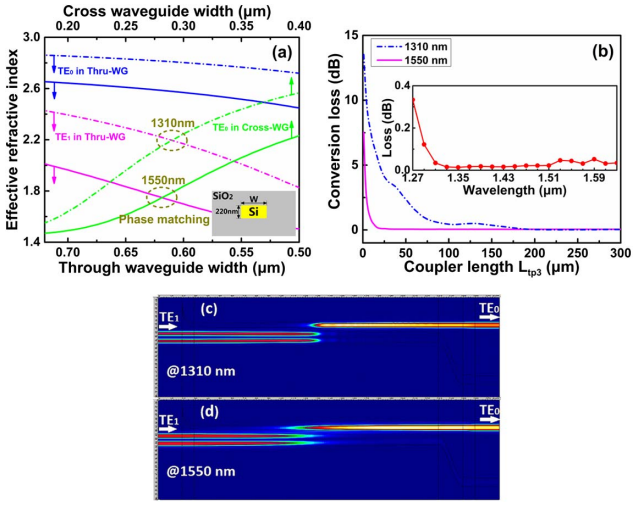

Fig. 4. (a) The calculated effective refractive indices of the modes (TE_0/TE_0 and TE_1) in the cross/through waveguide of the counter-tapered coupler with width tapering from 0.18/0.72 to 0.4/0.5 μm at wavelengths of 1310 nm (dashed) and 1550 nm (straight). (b) Mode conversion loss from the launched TE_1 mode to the TE_0 mode at the wavelengths of 1310 and 1550 nm. Inset: wavelength dependence of the mode conversion loss at $L_{tp3} = 200$ μm and $W_g = 0.16$ μm. (c) and (d) Simulated electric field intensity distributions in the counter-tapered coupler as the TE_1 mode launched at the wavelengths of 1310 and 1550 nm, respectively. $W_7 = 0.45$ μm.

the TE_0 mode in the cross waveguide at the two wavelengths of 1310 and 1550 nm, as shown in Fig. 4(a). The width of the through waveguide decreases from 0.72 μm (W_3) to 0.5 μm (W_4), whereas the width of the cross waveguide increases from 0.18 μm (W_5) to 0.4 μm (W_6). Effective index cross points or phase-matching points between the TE_1 mode in the through waveguide and the TE_0 mode in the cross one can be found in Fig. 4(a) for both wavelengths of 1310 and 1550 nm; these are circled by brown dashed lines. This indicates the TE_1 mode in the through waveguide would convert to the TE_0 mode in the cross one with a properly designed coupler length L_{tp3}. The end widths of the two tapers are carefully selected to ensure not only the existence of index cross points, but also that no converted modes couple back. Unexpected coupling between the two TE_0 modes in through and cross WGs is eliminated with a larger through WG width W_4.

The taper length is also an important factor in selecting the taper end width. Figure 4(b) shows the simulated mode conversion loss as the function of coupler length L_{tp3} at the wavelengths of 1310 and 1550 nm. The mode conversion loss decreases as L_{tp3} increases, and a very low loss of less than 0.1 dB can be achieved when $L_{tp3} >$ 190 μm at both wavelengths of 1310 and 1550 nm. An L_{tp3} of 200 μm is selected considering the device loss and footprint. Conversion losses are finally simulated with FIMMPROP and shown in the inset of Fig. 4(b). Losses less than 0.2 dB can be obtained in the wavelength range from 1.29 to 1.63 μm. A larger coupler length would further reduce the conversion loss of modes with wavelengths

smaller than 1310 nm. Figures 4(c) and 4(d) show the simulated electric field intensity distribution in this counter-tapered coupler with the TE_1 mode launched at wavelengths 1310 and 1550 nm, respectively. One can note that the mode conversions from the TE_1 mode to TE_0 mode in this coupler are achieved as expected. For TE_0 mode input, it will pass through the coupler directly, as no index cross points and mode coupling occur between the two waveguides.

FIMMPROP is used to verify the performance of the complete device. The PRS device performances are usually characterized by IL and CT for each input polarization. Figure 5(a) shows the wavelength dependence of the IL and CT for the TE_0 mode and TM_0 mode. CT and IL of less than −15 and −0.2 dB are obtained from the wavelength of 1290 to 1610 nm for both input modes, respectively. With such a broad operating bandwidth, this device offers great potential in silicon photonic systems, especially in applications requiring a large operation waveband, such as WDM PONs for FTTH. Figures 5(b)–5(g) show the simulated electric field intensity distribution in the designed PRS at the wavelengths of 1310, 1490, and 1550 nm. For all three wavelengths, the launched TM_0 modes output from the cross port of the PRS after conversion to the TE_0 modes. Meanwhile, the input TE_0 modes output from the through port directly, which confirms our previous design.

The IL and CT gradually degrade for the TM_0 mode input when the wavelength falls short of 1310 nm, as shown in Fig. 5(a), but this can be improved by increasing the coupler length L_{tp3} of the counter-tapered coupler. Meanwhile, the CT of the TM_0 mode has some ripples that can be improved by increasing the lengths L_{tp1} and L_{tp2} of the bi-level taper. The CT gradually increases with the increasing wavelength for both two modes, which is caused by the coupling between the S-type output waveguide and straight output that can be further improved by design optimization.

The fabrication tolerance is investigated for the proposed PRS. Performance degradations for the TM_0 and TE_0 mode inputs are simulated. Figures 6(a)–6(c) show the wavelength dependence of the IL and CT with a top silicon thickness variation of ΔH, a slab height variation of Δh, and a waveguide width variation of ΔW, which includes the bi-level taper and counter-tapered coupler as the TM_0 mode input. The performance metrics remain stable with a width variation of ±40 nm and top silicon thickness or slab height variation of ±10 nm in the whole operation waveband. As no mode conversion and coupling occur in the PRS for the TE_0 mode input, the performance metrics remain stable with the above variation for the TE_0 mode input through our simulation. Manufacturing deviations with a top silicon thickness variation of ±5 nm and linewidth variations <1% are demonstrated in silicon photonic platforms[11,12], which are smaller than the fabrication tolerances of the design. Due to the adiabatic conversion and coupling of modes in the bi-level taper and counter-tapered coupler, the width, thickness, or wavelength variation only lead to the position shift of the mode

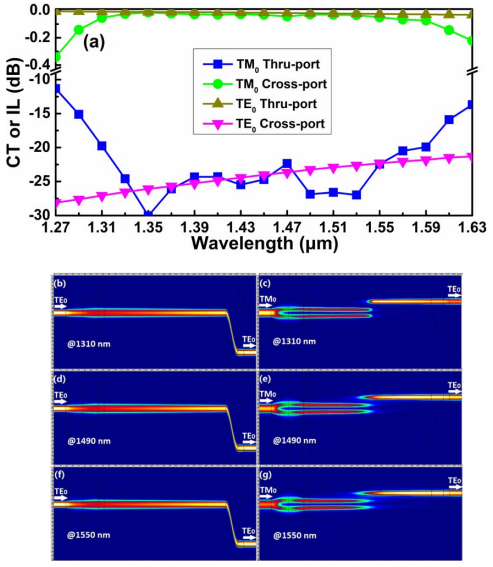

Fig. 5. (a) Wavelength dependence of the PRS performance in terms of the IL and CT for different launched modes. (b)–(g) Simulated electric field intensity distributions in our proposed PRS as the TE_0 mode and TM_0 mode launched at the wavelengths of 1310, 1490, and 1550 nm.

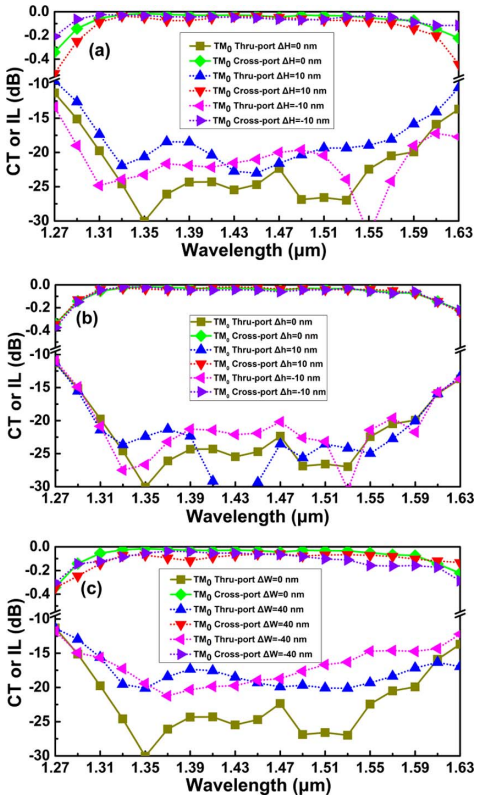

Fig. 6. Fabrication tolerance analysis for the wavelength dependence of IL and CT with (a) the top silicon thickness variation ΔH, (b) the slab height variation Δh, and (c) the waveguide width variation ΔW of the whole device as the TM_0 mode launched.

hybridizations and phase-matching points and will not affect the PRS performance seriously. Compared to the previously reported PSGC[17] and PRS[8], this device has an ultra-broad operating bandwidth and large fabrication tolerance, which offers potentials in applications requiring a large operation bandwidth such as WDM PONs for FTTH.

In addition, only the mode conversion loss is considered in this work. The scattering loss due to the side-wall roughness of the waveguide is extremely detrimental to the total loss of this PRS in practice. This kind of loss could be significantly reduced by optimizing the fabrication process, such as photolithography and etching processes[18]. To further reduce the size, a narrower gap of W_g could be selected to enhance the coupling strength, and thus, a smaller coupler length L_{tp3} can be obtained. On the other hand, the bi-level tapers could be optimized by adopting some other shapes (e.g., parabolic or sinusoidal) with multi-variable optimization[19] to reduce the device length.

In conclusion, an ultra-broadband and fabrication-tolerant silicon PRS based on a cascaded adiabatic taper and mode-evolution counter-tapered coupler is proposed in this Letter. IL and CT of less than 0.2 and −15 dB are obtained, respectively, with a bandwidth as large as 320 nm. Due to the asymmetric cross section of the rib waveguide, a standard SiO_2 top cladding is used, eliminating the need for silicon nitride or air cladding. The performance degradation due to fabrication errors is also analyzed, showing that the device is quite robust, with tolerances greater than the manufacturing deviations of mature silicon photonic platforms. With such a broad operating bandwidth and robust performance, this device offers great potential in silicon photonic systems, especially in applications requiring large bandwidths such as WDM PONs for FTTH.

This work was supported by the National Natural Science Foundation of China (Nos. 61275112, 61475180, and 11204340), the Science and Technology Commission of Shanghai Municipality (No. 14JC1407600), and the Shanghai Natural and Science Foundation (No. 16ZR1442600).

References

1. D. Xu, J. H. Schmid, G. T. Reed, G. Z. Mashanovich, D. J. Thomson, M. Nedeljkovic, X. Chen, D. V. Thourhout, S. Keyvaninia, and S. K. Selvaraja, J. Sel. Top. Quantum Electron. **20**, 422 (2014).
2. P. P. Absil, P. Verheyen, P. De Heyn, M. Pantouvaki, G. Lepage, J. De Coster, and J. Van Campenhout, Opt. Express **23**, 9369 (2015).
3. Y. Fu, T. Ye, W. Tang, and T. Chu, Photon. Res. **2**, A41 (2014).
4. J. Xing, Z. Li, P. Zhou, Y. Gong, Y. Yu, M. Tan, and J. Yu, Chin. Opt. Lett. **13**, 061301 (2015).
5. M. Streshinsky, R. Ding, Y. Liu, A. Novack, C. Galland, A. E.-J. Lim, P. G.-Q. Lo, T. Baehr-Jones, and M. Hochberg, Opt. Photon. News **24**, 32 (2013).
6. A. Dewanjee, J. N. Caspers, D. F. V. James, and M. Mojahedi, in *Photonics Conference (IPC)*, 560 (2014).
7. J. Zhang, J. Yang, H. Lu, W. Wu, J. Huang, and S. Chang, Chin. Opt. Lett. **13**, 091301 (2015).
8. H. Guan, Q. Fang, G.-Q. Lo, and K. Bergman, IEEE Photon. Technol. Lett. **27**, 518 (2015).
9. J. Wang, B. Niu, Z. Sheng, A. Wu, W. Li, X. Wang, S. Zou, M. Qi, and F. Gan, Opt. Express **22**, 13565 (2014).
10. L. Socci, V. Sorianello, and M. Romagnoli, Opt. Express **23**, 19261 (2015).
11. A. V. Krishnamoorthy, X. Zheng, G. Li, J. Yao, T. Pinguet, A. Mekis, H. Thacker, I. Shubin, Y. Luo, K. Raj, and J. E. Cunningham, IEEE Photon. J. **3**, 567 (2011).
12. W. Bogaerts, S. K. Selvaraja, P. Dumon, J. Brouckaert, K. De Vos, D. Van Thourhout, and R. Baets, J. Sel. Top. Quantum Electron. **16**, 33 (2010).
13. A. E. J. Lim, J. Song, F. Qing, C. Li, X. Tu, N. Duan, K. K. Chen, R. P. C. Tern, and T. Y. Liow, J. Sel. Top. Quantum Electron. **20**, 405 (2014).
14. D. Dai, Y. Tang, and J. E. Bowers, Opt. Express **20**, 13425 (2012).
15. A. F. Milton and W. K. Burns, Appl. Opt. **14**, 1207 (1975).
16. N. Riesen and J. D. Love, J. Lightwave Technol. **31**, 2163 (2013).
17. M. Streshinsky, R. Shi, A. Novack, R. T. Cher, A. E. Lim, P. G. Lo, T. Baehr-Jones, and M. Hochberg, Opt. Express **21**, 31019 (2013).
18. C. Qiu, Z. Sheng, H. Li, W. Liu, L. Li, A. Pang, A. Wu, X. Wang, S. Zou, and F. Gan, IEEE/OSA J. Lightwave Technol. **32**, 2303 (2014).
19. B. Luyssaert, P. Vandersteegen, D. Taillaert, P. Dumon, W. Bogaerts, P. Bienstman, D. Van Thourhout, V. Wiaux, S. Beckx, and R. Baets, IEEE Photon. Technol. Lett. **17**, 73 (2005).